The effect of water vapor on surface oxygen exchange kinetics of thin film (La,Sr)(Co,Fe)O$_{3-\delta}$

Dongwei Xu [a,3,1], E. Mitchell Hopper [a,3], Kee-Chul Chang [a], Peter M. Baldo [a], Haesun Park [a], Jeffrey A. Eastman [a], Hoydoo You [a], Paul H. Fuoss [a,2], Brian J. Ingram [b,*], Peter Zapol [a,**]

[a] Materials Science Division, Argonne National Laboratory, Lemont, IL, 60439, USA
[b] Chemical Sciences and Engineering Division, Argonne National Laboratory, Lemont, IL, 60439, USA

HIGHLIGHTS

- Model thin film surfaces used to probe environmental effects on fuel cells.
- Chemical induced strain established by high energy X-ray diffraction studies.
- Combined computational and experimental analysis of oxygen ion transport.
- Water vapor may promote the oxygen reduction reaction at perovskite surfaces.

GRAPHICAL ABSTRACT
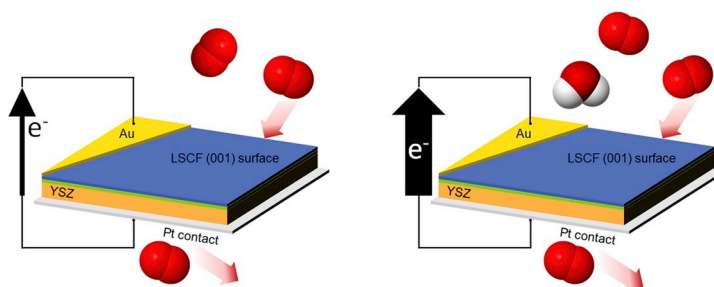
ARTICLE INFO

ABSTRACT

Oxygen reduction and transport in electrochemical applications are strongly affected by the reactant gas composition, including impurities such as water. Understanding the relationship between oxygen reactivity and humidity is key for attaining stability and high efficiency of solid oxide fuel cells, which are especially attractive for transportation applications as low emission power generation devices. Both short- and long-term effects of moisture have previously been associated with use of ambient air. To better understand these effects, we study oxygen exchange kinetics at the cathode surface and the cathode/electrolyte interface using La$_{0.6}$Sr$_{0.4}$Co$_{0.2}$Fe$_{0.8}$O$_{3-\delta}$ (LSCF) epitaxial thin films as a model-surface system. In situ synchrotron X-ray techniques evaluate the oxygen reduction reaction (ORR) kinetics in response to environmental variables. The results suggest a clear enhancement of the ORR rate upon short term exposure of the perovskite-structured films to water. On the basis of these measurements, along with in situ X-ray characterization of Sr segregation and computational first-principles studies, we suggest a model for this increased ORR activity that may lead to further improvements by stabilizing active cathode surface configurations.

1. Introduction

Complex redox reactions and charge transfer [1,2] are electrochemical phenomena that play critical roles in many fields from biology and corrosion to energy storage and conversion devices. The oxygen reduction reaction (ORR) is a key electrochemical reaction that has attracted much fundamental interest in elucidating reaction mechanisms at gas/solid interfaces. Relationships between activity and stability of electrocatalytic materials for the ORR require further fundamental understanding in order to improve both simultaneously. Solid oxide fuel cells (SOFCs), which are efficient devices that generate electricity from controlled oxidation of an available fuel (e.g., hydrogen), rely on the ORR to generate oxygen ions, and a solid oxide-ion conducting ceramic to transport the oxide ions to oxidize a fuel source. SOFCs are of particular interest due to their fuel flexibility and high efficiencies – especially as a combined heat and power system to generate electric and thermal energy, but they presently require operating temperatures above 700 °C.

The ORR rate and efficiency are the limiting factors in overall SOFC performance, especially at desired lower operating temperatures. How a variety of chemical and physical phenomena affect the reaction efficiencies is not fully understood. For instance, humidity in ambient air is known to affect short- and long-term ORR behavior [3,4]. The elevated temperatures required to increase solid-state oxygen ion conduction and overcome sluggish ORR kinetics contribute to additional materials and chemical challenges. Research efforts are driven by the desire to maintain ORR efficiency and enable robust charge transfer mechanisms at lower operating temperatures, under variable ambient environments.

Lanthanum based perovskites, e.g., strontium-doped lanthanum cobalt ferrite (LSCF), are established ORR electrochemical catalysts typically utilized as intermediate temperature (600–800 °C) SOFC cathodes for operation in ambient air [5]. The stability of LSCF under realistic operating conditions has been studied to address issues hampering practical applications. Over long time scales (>1000 h), there is consensus that reactions in humid air cause fuel cell performance to degrade more rapidly relative to dry air [4,6–13]. For instance, water exacerbates the segregation of Sr species to the LSCF surface in the presence of CO_2, thereby decreasing the ORR activity [14–16], enhancing decomposition or component reactions [6,9], or contributing to the transport of volatile chromium or silicon species [11–13].

In addition to its indirect role in ORR via long-term degradation mechanisms, humidity plays a direct role in ORR by controlling oxygen surface exchange coefficient kinetics on LSCF and related lanthanum-based perovskite-type materials. Minor gas phase components such as water vapor are known to take part in surface reactions and interact directly with perovskite surfaces [3]. Among different techniques, isotope exchange depth profiling and gas analysis are valuable techniques used to investigate surface exchange of oxygen and H_2O [3,7,17,18]. In contrast to long-term degradation processes, studies on the short-term effects of H_2O on the oxygen surface exchange coefficient (k_{chem}) have reached differing conclusions; the exchange coefficient is found to decrease in some reports [7,8,17,18] but increase in others [13,17,19]. Some of the discrepancies can be explained by the lack of full correspondence between experimentally determined oxygen tracer exchange coefficients, and electrochemical oxygen exchange due to uncertainty in limiting reaction kinetics [17]. New, complementary techniques to assess oxygen exchange kinetics will help to resolve the role of humidity in short term ORR behavior.

In previous work by our group, we developed an in situ method to extract relative oxygen exchange kinetics at an LSCF surface and buried LSCF/Gd_2O_3-doped CeO_2 (GDC) and GDC/Y_2O_3-stabilized ZrO_2 (YSZ) interfaces by using synchrotron X-rays to measure the lattice response to applied potentials across a thin film heterostructure [20,21] used as a model SOFC cathode/electrolyte system. This allowed us to characterize various steps in the ORR on idealized metal-oxide surfaces. Herein, we describe an extension of this approach to measure the relative changes in

oxygen transfer kinetics under environmental perturbations. Namely, we use in situ synchrotron X-ray measurements to investigate the effect of H_2O on the ORR at an LSCF thin film surface while driving oxygen through the LSCF/GDC/YSZ heterostructure, which provides a measure of oxygen exchange. Along with X-ray fluorescence characterization of Sr segregation and first-principles computational studies of the interaction of water species with oxygen vacancies, we observe increased ORR activity related to short time scale water exposure and propose a model consistent with this behavior.

2. Experimental and computational methods

LSCF films are fabricated by pulsed laser deposition as described in our previous report [21]. Targets with nominal compositions of $La_{0.6}Sr_{0.4}Co_{0.2}Fe_{0.8}O_{3-\delta}$ and $Ce_{0.8}Gd_{0.2}O_{1.9}$ are used to deposit 60 nm LSCF and 5 nm GDC films, respectively, on single crystal (001)-oriented YSZ substrates. Both the GDC and LSCF films are epitaxially oriented relative to the YSZ substrate such that (001) YSZ∥(001) GDC∥(001) LSCF and [100] YSZ∥[100] GDC∥[110] LSCF. The LSCF orientation is described using pseudocubic indices (with a = b = c ≈ 3.9 Å). X-ray diffraction characterization is used to confirm the phase purity and orientation relationships, and the film surface roughness is determined to be below 1 nm by atomic force microscopy (see Fig. S1).

Fig. 1 shows a schematic of the sample heterostructure geometry and design. Thin film sample geometry allows the unique capability of Total X-ray Reflection Fluorescence (TXRF) [22] to measure surface composition ratios at the temperatures and applied potentials relevant to the SOFC operating conditions. The experimental setup [23] allows us to collect X-ray fluorescence ratios at the glancing X-ray incidence angle corresponding to total external reflection, while simultaneously characterizing electrochemical behavior. In order to observe in-plane and out-of-plane lattice strains simultaneously, the non-specular LSCF (111) diffraction peak is continuously monitored with a 1° incidence angle of the X-rays onto the sample. A gold current collector is screen printed on the LSCF surface, oriented such that the incident X-rays are parallel to the current collector edge when the sample orientation satisfies the LSCF (111) Bragg condition for the 16.725 keV X-ray energy used. The incident X-ray beam width on the sample is confined to 20–50 μm parallel to the long edge of the top current collector using slits and a vertically focusing mirror. It should be noted that in these experiments, the incident beam was aligned approximately 0.1–1 mm from the edge of the gold current collector (see Fig. 1). Since the local voltage observed between the LSCF surface and platinum counter electrode decreases exponentially as a function of lateral distance from the gold current collector (see Fig. S2), this X-ray beam size and position ensures that the measurements reflect the local properties of the sample. Additionally, locating the incident beam ~1 mm from the edge of the gold current
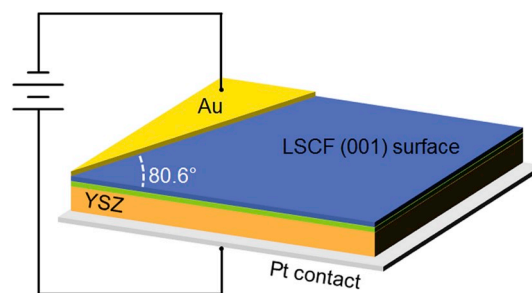
Fig. 1. Epitaxial heterostructures of 60 nm LSFC and 5 nm GDC layers, representing model SOFC systems, were fabricated by pulsed laser deposition. The X-ray beam was aligned parallel to the edge of a screen printed gold current collector angled 9.4° relative to the [100] substrate edge (satisfying the LSCF (111) Bragg condition). A platinum current collector mesh is used on the reverse YSZ surface. (For interpretation of the references to colour in this figure legend, the reader is referred to the Web version of this article.)

collector minimizes the effects of misalignment and beam width. The LSCF surface potential at this position is estimated to be 10–15% of the applied voltage. The gold current collector edge is determined by mapping the Au fluorescence signal, and once determined, the sample is translated orthogonal to the Au edge by a desired distance. A Pilatus 100 K area detector acquires images of the diffracted beam intensity every 100 ms, allowing for high temporal resolution of structural relaxation upon applying an electric potential. A screen-printed platinum current collector covers the entire reverse side of the YSZ substrate to enable through-plane conduction measurements.
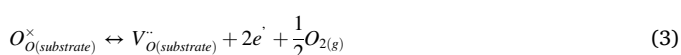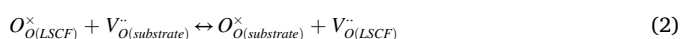
An electrical potential is applied across the heterostructure by connecting the metal (Au/Pt) current collectors to a Keithley 2400 Source Meter. The heterostructures are mounted on a ceramic heater in an environmental chamber on a diffractometer at Sector 12ID-D of the Advanced Photon Source [24]. The total chamber pressure is maintained at 150 Torr, and variable oxygen/helium gas mixtures are used to control the oxygen partial pressure (pO$_2$) between 1.5 and 150 Torr. H$_2$O is introduced by passing the O$_2$/He gas mixture through a thermally controlled bubbler at a controlled pressure and flow rate; the pH$_2$O was verified with a mass spectrometer on the outlet of the X-ray chamber. The sample heater set points are 350 °C–600 °C, with actual sample surface temperatures approximately 10–20% lower as calibrated by contacting a type-S thermocouple to the surface.

First-principles calculations of the relative formation energies of oxygen vacancies are used to interpret the acquired experimental results. Density functional theory (DFT) calculations are carried out using the projector augmented plane-wave (PAW) method, as implemented in the Vienna ab initio simulation package (VASP) [25,26]. The generalized gradient approximation (GGA) of Perdew, Burke and Ernzerhof (PBE) is adopted for the exchange–correlation functional [27] and the B-site transition metal elements are treated by the PBE + U method with U_{eff} = 5.1 eV and 3.3 eV for Fe and Co, respectively [28–30]. We have also tested U_{eff} = 4.0 eV for both Fe and Co [31]. The $3d^74s^1$ and $3d^84s^1$ electrons of Fe and Co atoms are considered as the valence electrons. We restrict our calculations to G-type anti-ferromagnetic (AFM) ordering of the transition metal cations, which was previously determined to be the ground state of LaFeO3 [32]. The initial absolute values of the magnetization were set to 4 μB and 2.98 μB for Fe and Co, respectively [29,31, 33].

A periodic slab model for surface calculations is used with a vacuum distance of at least 15 Å between neighboring images along the surface normal direction. The energy cut-off for the plane-wave basis set is set to 400 eV. The total energy is converged with a tolerance of 10^{-5} eV in the iterative solution of the Kohn–Sham equations. The atomic positions are relaxed until the force on each atom is less than 0.02 eV/Å. A 5 × 5 × 1 Monkhorst–Pack mesh is used for the Brillouin-Zone integrations.

3. Results and discussion

We investigated the ORR using the experimental geometry shown in Fig. 1, with an electric field applied across the current collector on the YSZ electrolyte (bottom surface) to the surface of the LSCF thin film (top surface). A cathodic potential results in oxygen reduction involving four electrons per O$_2$ molecule at the LSCF surface and subsequent oxygen transport across the surface, LSCF film, buried LSCF/GDC and GDC/YSZ interfaces, and the YSZ substrate as described by the forward reactions in Eqs. (1) and (2). Redox of the LSCF B-site cations, as described in detail elsewhere [20,21], is implied in Eq. (1).

$$\frac{1}{2}O_{2(g)} + V^{\cdot\cdot}_{O(LSCF)} + 2e^{\cdot} \leftrightarrow O^{\times}_{O(LSCF)} \tag{1}$$

$$O^{\times}_{O(LSCF)} + V^{\cdot\cdot}_{O(substrate)} \leftrightarrow O^{\times}_{O(substrate)} + V^{\cdot\cdot}_{O(LSCF)} \tag{2}$$

$$O^{\times}_{O(substrate)} \leftrightarrow V^{\cdot\cdot}_{O(substrate)} + 2e^{\cdot} + \frac{1}{2}O_{2(g)} \tag{3}$$

In Eqs. (2) and (3), "substrate" refers to the YSZ/GDC portion of the heterostructure. The different relative rates of oxygen transport across the LSCF surface and buried LSCF/GDC interface result in dissimilar oxygen flux in and out of film. Under a cathodic potential, faster oxygen transport across the buried GDC/LSCF interface relative to the LSCF surface results in buildup of oxygen vacancies within the LSCF film.

This change in vacancy concentration, i.e., $[V^{\cdot\cdot}_O]$, can be monitored with high temporal resolution via lattice expansion [34–36] measured by X-ray diffraction. The out-of-plane lattice parameter varies linearly with $[V^{\cdot\cdot}_O]$; therefore, the time-dependent strain, ξ(t), is related to the oxygen vacancy fraction, C, which is a dimensionless fraction of vacant oxygen sites (i.e., the ratio of $[V^{\cdot\cdot}_O]$ to the total oxygen site concentration, C_{tot}):

$$\frac{\xi(t)}{\xi_\infty} = \frac{C(t) - C_0}{C_\infty - C_0} = 1 - exp\left[-\left(\frac{K^{'}}{d}\right)t\right] \tag{4}$$

where ξ_∞ and ξ(t) are the steady state (t → ∞) and instantaneous out-of-plane strains in the LSCF film, respectively, K' is an effective rate constant, d is the LSCF film thickness, and the electric field is applied at t = 0. Steady state conditions typically are reached at t = 10–30 s, dependent on factors such as the sample temperature.

Our previous results described the relationship between the $[V^{\cdot\cdot}_O]$ and applied electric field in LSCF thin film heterostructures [20,21]. The difference between the steady-state (t → ∞) and initial thermodynamic equilibrium (t = 0) oxygen vacancy concentrations, (C$_\infty$ – C$_0$) is proportional to ξ_∞, and is a measure of the relative oxygen transport rates across the two interfaces. The time dependence of strain, ξ(t), under applied electric field is described by K', as indicated in Eq. (4), which is the summation of the rate constants for the forward directions of Eqs. (1) and (2) (cathodic applied potentials) and is dominated typically by the surface reaction, i.e., Eq. (1) [21]. By monitoring the instantaneous strain, ξ(t), and determining the steady-state strain, ξ_∞, under operando conditions, the role of chemical or structural perturbation of the LSCF surface on the oxygen reduction reaction rate can be analyzed using Eq. (4).

A baseline in the present study was established by continuously monitoring the instantaneous strain ξ(t), electrical resistance, and cation surface composition at various temperatures, humidity levels (at constant 150 Torr total pressure, 15 Torr O$_2$, Ar balance), and cathodic electric fields (i.e., driving the forward direction of Eqs. (1) and (2)). A typical result is shown in Fig. 2, which compares relaxation curves after applying a cathodic potential at t = 0 s in dry vs. pH$_2$O = 6 Torr conditions. The data is normalized to the steady-state strain (ξ_∞) achieved during dry conditions. For all conditions discussed herein, lattice strain in response to an applied field was verified to occur only in the [001] direction, i.e., perpendicular to the surface; no in-plane strain was observed due to the constraints imposed by the substrate. Fig. 2 indicates the instantaneous lattice strain, ξ(t), follows an exponential relaxation function characterized by an effective rate constant (K') as described by Eq. (4) [21]; K' increases under pH$_2$O = 6 Torr vs. 0 Torr (dry) conditions. Furthermore, the resulting steady-state lattice strain (ξ_∞) upon application of a cathodic potential (as t → ∞) decreases approximately 60% at pH$_2$O = 6 Torr vs. dry conditions. It should be noted that K' is largely independent of the initial $[V^{\cdot\cdot}_O]$ in the LSCF layer; whereas, the magnitude of the steady-state strain is given by the ratio of the change to initial $[V^{\cdot\cdot}_O]$ in the LSFC layer [21]. The induced strain is reversible (i.e., returns to initial lattice parameters) at equilibrium conditions upon removal of the electric field with comparable exponential decay rates.

The out-of-plane steady-state strain ξ_∞ induced by the cathodic electric field is shown in Fig. 3a as a function of time under water exposure, t$_w$. Each datum in Fig. 3a corresponds to the steady-state value achieved (t → ∞) upon application of an electric field (as described in Fig. 2); between each datum, the system was allowed to completely relax to equilibrium conditions at E = 0 V. Fig. 3a indicates a constant
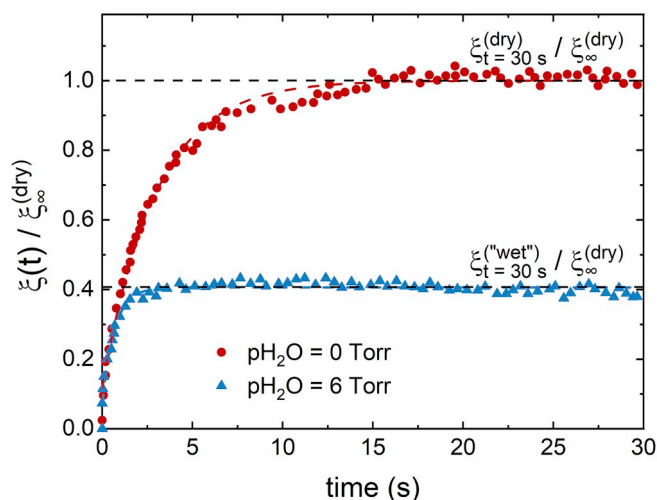
Fig. 2. A comparison of typical stain responses under dry vs. $pH_2O = 6$ Torr conditions as a function of time in which a cathodic potential of -1.5 V is applied at $t = 0$ s. The values are normalized to the steady-state strain (ξ_∞) achieved during dry conditions ($\xi_\infty^{(dry)}$). The response can be fit with Eq. (4) to determine an effective rate constant.
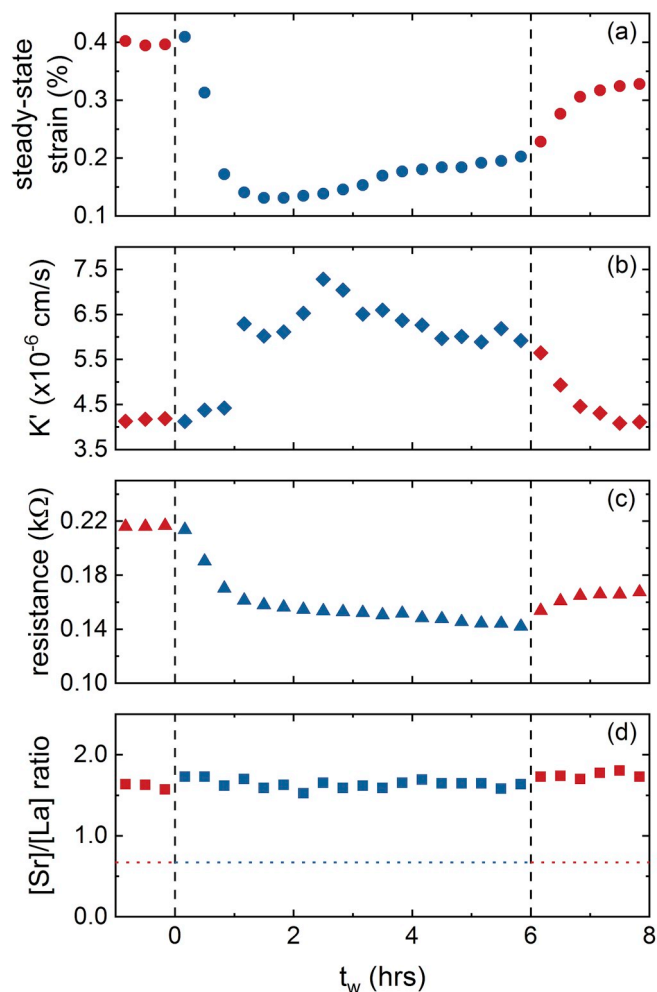

Fig. 3. (a) Steady-state strain at -1.5 V at 600 °C and 15 Torr pO_2, (b) rate constant calculated using Eq. (4) from strain time dependence after applying voltage at each point, (c) sample resistance, and (d) surface [Sr]/[La] ratio with addition ($t_w = 0$ h) and removal ($t_w = 6$ h) of 6 Torr H_2O to the measurement atmosphere (the dotted line represents the nominal bulk [Sr]/[La]).

reversible response of $\xi_\infty \approx 0.4\%$ at $t_w < 0$ h (dry conditions). Upon introduction of 6 Torr H_2O (maintaining $pO_2 = 150$ Torr total pressure) at $t_w = 0$ h, ξ_∞ decreases from 0.4% under dry conditions to 0.1–0.2% under wet conditions, suggesting that the relative rates of oxygen transport across the air/LSFC surface and the buried LSCF/GDC interface vary due to exposure of the film surface to water vapor. Furthermore, we assume the buried interfacial structure and chemistry remains unchanged; therefore, the results from Fig. 3a imply that the LSCF surface becomes less limiting to oxygen exchange upon exposure of to water vapor. In other words, the oxygen flux across the interface, i.e., annihilation of oxygen vacancies, is facilitated such that ξ_∞ is significantly reduced under wet conditions.

The effective relaxation time constant, K′ calculated from Eq. (4) is shown in Fig. 3b. The forward rate constant of Eq. (1) (LSCF surface ORR reaction) dominates K′ relative to the contribution from the forward direction of Eq. (2) (buried interface oxygen transport) [21]; therefore, the rate constant in Fig. 3b can be considered a measure of the ORR rate. The presence of H_2O clearly increases the effective rate constant, which is consistent with the findings in Fig. 3a.

Furthermore, the cell resistance, as shown in Fig. 3c, is commensurately reduced, as expected from improved oxygen transport kinetics described in Fig. 3a and b. It should be noted that the reported resistance values are not normalized for surface area due to the complex potential distribution with respect to the current collector position and high sheet resistance (see Fig. S2). As such, the resistance values reported in Fig. 3c average a broad distribution of surface potentials; whereas, the crystallographic strains analyzed in Fig. 3a and b are isolated to regions near the current collectors (i.e., ~20–50 μm probe width located approximately 1 mm from the Au current collector).

Since both ξ_∞ and cell resistance are dependent on the initial ($t_w < 0$ h) absolute $[V_O^{\cdot\cdot}]$ [21], it may be the case that longer times are required after removing H_2O exposure (at $t_w = 6$ h) to restore the initial values observed at dry conditions ($t_w < 0$ h), as seen in Fig. 3a and c. This is compared to K′, which is independent of the absolute $[V_O^{\cdot\cdot}]$ in the LSCF layer [21] and and returns rapidly to dry conditions ($t_w < 0$ h) upon ending H_2O exposure (at $t_w = 6$ h).

Fig. 3d presents the ratio of [Sr]/[La] at the surface (<5 nm deep, determined by TXRF measurements slightly below the critical X-ray incidence angle), where the X-ray penetration depth into the sample is limited to within a few nanometers of the surface. The bulk composition (dotted line at [Sr]/[La] = 0.67) is determined from fluorescence measurements using a larger incidence angle that results in total penetration of the X-ray beam through the film thickness. Strontium segregation to the surface of LSCF thin films (as well as bulk powders) is described throughout the literature [15,37–39] and is consistently observed in the experiments described here. Significant Sr surface segregation is induced by the exposure of the LSCF film to operando thermal conditions, but the surface Sr concentration is not observed to change over the time interval of the current experiments or upon application of electric fields, nor were secondary phases detected on the surface. Therefore, a change in the surface Sr concentration is ruled out as a significant contributor to the observed lattice changes under applied potential. Furthermore, although Co surface enhancement has been reported [23], no time or potential dependence of B-site surface cation concentration was observed.

Previous computational DFT studies [40,41] addressed differences in O exchange reactions on AO and BO_2 terminated (001) surfaces of ABO_3 perovskites without looking at the effects of water. It was found that the kinetics is at least two orders of magnitude faster on BO_2 termination than on AO termination and suggested that long-term annealing results in Sr enrichment and thus potential loss of much less stable BO2 termination, consistent with experimental long-term behavior. Our experimental results indicate in Fig. 3d indicate Sr enrichment that remains stable over the time of experiments. For AO termination, previously calculated vacancy formation energy for vacancies the central layers of the LSMO slab was found to be more favorable than for

vacancies on (La,Sr)O surfaces [40]. Other computational results [41] for dry Sr-rich (001) surface in LSCO were found to be consistent with experiments and Sr enrichment was found to be critical for good performance on AO termination.

We use first-principles calculations to explore the mechanism of the water-induced enhancement of the electrochemical oxygen reactions shown in Fig. 3. The structure of bulk $LaFe_{0.75}Co_{0.25}O_3$ is modeled using optimized lattice parameters of a = b = c = 3.889 Å with cubic symmetry. When Sr is introduced to the system, oxygen vacancies are expected to compensate the divalent Sr substitution of trivalent La ions. Thus, substitution of two Sr ions will introduce one oxygen vacancy without requiring a valence change of the transition metal ions; therefore, 50% Sr substitution of the La sites results in a bulk composition of $La_{0.5}Sr_{0.5}Fe_{0.75}Co_{0.25}O_{2.75}$. Since the results in Fig. 3 were obtained using films grown with a (001) surface orientation and a strong Sr enrichment of the surface both with and without water exposure, a Sr-enriched (001) surface is considered in the computational model.

Because of our experimental observations illustrated in Fig. 2d and the previously reported observations of Wachsman et al. [36], we use a model with the Sr concentration on the surface twice that in the bulk. To create the simplest model that includes Sr segregation, we adopt a 2 × 2 surface supercell with 5-layer periodic slabs of Sr–O-terminated surfaces and validate our result using 9-layer periodic slab model. The lattice vectors of the cell are constrained to tetragonal symmetry with the in-plane lattice parameters a = b = 7.777 Å. All internal degrees of freedom are allowed to relax. In the absence of oxygen vacancies, the atomic compositions of the five layers in the supercell from the top are Sr_4O_4 - Fe_3CoO_8 – $La_2Sr_2O_4$ – Fe_3CoO_8 – Sr_4O_4, and the slab is symmetric. By introducing Sr segregation to the surface, three oxygen vacancies must be added to the system in order to maintain overall charge neutrality. If these are added symmetrically, e.g. one vacancy in 1, 3, and 5 layer each, there is no overall dipole moment for the slab. Otherwise, there could be a change in the local dipole between neighboring atomic planes in the slab that destroys the symmetry. There is no formal charge difference, however, between two surfaces of the slab that would result in an electric field inside the slab that diverges with slab thickness. There are several possible locations to consider in placing these vacancies, which are divided into two classes, (1) vacancies in the (Sr, La)O layers only and (2) vacancies distributed both in the (Fe, Co)O and (Sr, La)O layers. In calculations of each class, the total number of oxygen vacancies in the bottom two layers are fixed, and either one vacancy is incorporated in the (Sr, La)O layer per unit cell for class (1) or one vacancy is incorporated in the (Fe, Co)O layer for class (2). We investigate three possible vacancy distributions, corresponding to 0, 1, or 2 oxygen vacancies in the surface atomic plane. Since the overall number of vacancies in the DFT calculations is kept fixed, only their distribution between the surface and the central layers of the slab is changing, a comparison to the experimental strain in Fig. 3a that is the result of changes in vacancy concentration is not performed. To explore the effect of water on the vacancy distribution and, therefore, performance of the LSCF, the change in thermodynamic stability of vacancy distributions in the system is determined. The water molecule included in the model is located either on top of the Sr atom or at the oxygen vacancy site on the LSCF surface. All these possibilities are considered in the calculations.

Structures are optimized with and without an adsorbed surface water molecule for different oxygen vacancy concentrations in the top SrO layer, ranging from 0% (no vacancy on the surface) to 50% (two vacancies in the top layer of the computational cell). The lowest energy structures for both cases, without water and with water adsorbed on the surface, are shown in Fig. 4a and b, respectively. The numbers arrayed vertically next to the structure and the numbers below the square symbols in Fig. 4c and d indicate the number of oxygen vacancies in each layer of the computational cell. We show all slab structures listed in Fig. 4c and d in Supplemental Information (Fig. S3) and absolute total energies for all slabs and water molecule in the gas phase in Table S1. Water molecule prefers a dissociated configuration on the SrO terminated LSCF surface as shown in Fig. 4b. One hydrogen from the water molecule binds to an oxygen atom on the LSCF surface forming two –OH bonds. Furthermore, the oxygen atom of the water does not fill a vacant oxygen site on the LSCF surface. The bond length between Fe and –OH is 3.57 Å, much larger than the distance between Fe and another O in the octahedron (~1.97 Å) (see Fig. 4).

The total electronic energies as a function of the number of surface oxygen vacancies $N_{V\ddot{O}}$ for the system without and with water are shown in Fig. 4c and d, respectively. We have tested other U_{eff} values (4.0 eV for
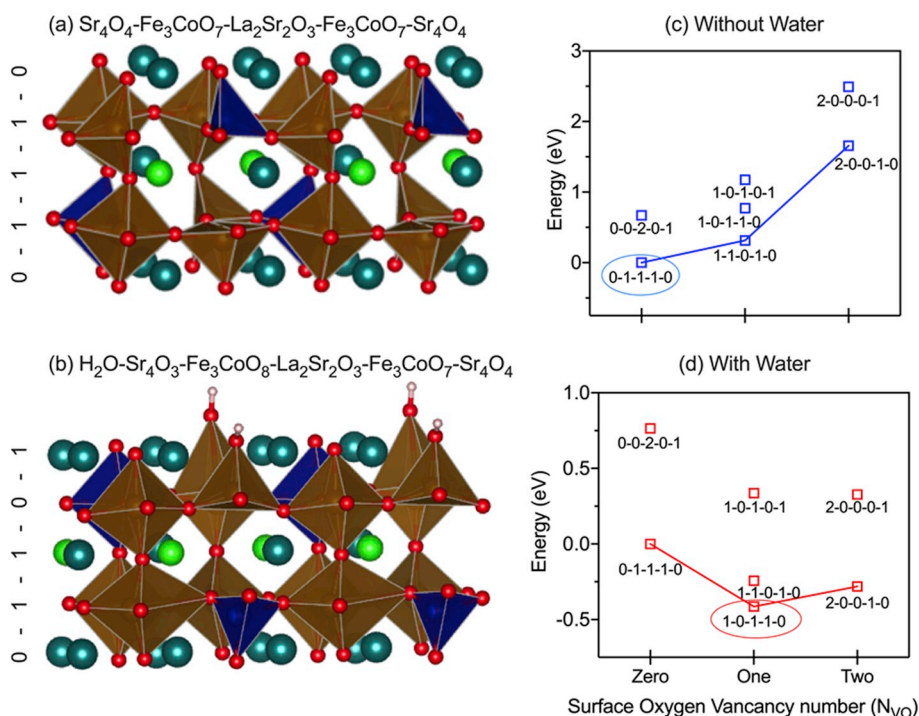
Fig. 4. The DFT-optimized structures corresponding to the lowest energy configurations of LSCF surface considered (a) without and (b) with a surface water molecule. The '0' and '1' array arranged vertically next to the structure indicates the number of oxygen vacancies in each layer. The dark green, green, blue, brown, red and light pink spheres represent Sr, La, Co, Fe, O and H atoms, respectively. The energies of possible configurations are sorted as a function of the number of surface oxygen vacancies (c) before and (d) after adding the surface H_2O molecule respectively. The five numbers next to the squares represent the oxygen vacancy number in each layer, beginning with the top layer. The lowest energy points circled in (c) and (d) correspond to the structures displayed in (a) and (b), respectively. (For interpretation of the references to colour in this figure legend, the reader is referred to the Web version of this article.)

(a) Sr_4O_4-Fe_3CoO_7-$La_2Sr_2O_3$-Fe_3CoO_7-Sr_4O_4

(b) H_2O-Sr_4O_3-Fe_3CoO_8-$La_2Sr_2O_3$-Fe_3CoO_7-Sr_4O_4

(c) Without Water

(d) With Water

Surface Oxygen Vacancy number (N_{VO})

both Fe and Co) using single point calculations on converged geometries (system without water) and the energy ordering among structures with different numbers of surface oxygen vacancies did not change. To check dependence of the relative energies on the slab thickness, we have also done calculations on a 9-layer slab that has 4 extra bulk-like layers, and the results are qualitatively the same as for the 5-layer slab, although they are slightly different numerically (see, Fig. S4). The two lowest energy structures are circled in the graph.

Without the water molecule on the surface, the energy increases with the number of surface vacancies, $N_{V\ddot{O}}$, as shown in Fig. 4c. This indicates that it is energetically unfavorable for oxygen vacancies to be on the SrO-terminated surface of LSCF in the absence of water molecules. With the water molecule present, however, the energy preference changes, and structures that include surface oxygen vacancies become more stable than structures with the same total number of vacancies distributed away from the surface.

Based on the above analysis, we hypothesize that OH groups are present on the surface if the gas atmosphere is humidified, which reduces the formation energy of oxygen vacancies on the surface, thus making it easier to activate oxygen and incorporate it into vacant lattice sites. In general, oxygen vacancies are beneficial for oxygen exchange kinetics [42]. This can explain the reversibility of the H_2O effect; once water is removed from the gas phase environment, the activation energy returns to its initial magnitude as –OH surface groups desorb. The fact that the initial performance before the addition of water is not completely recovered after water is removed suggests that a fraction of the –OH species remain adsorbed on the surface for times that exceed those probed in this experiment.

Sr surface enrichment was observed in this study, consistent with many other reports; the surface [Sr]:[La] ratio is over two times greater than in the nominal bulk ratio of the film (Fig. 3d). However, this occurs when the film is initially annealed under dry conditions and is unchanged throughout the rest of the experiment; most importantly, it is unaffected by the addition or removal of H_2O. Furthermore, $SrCO_3$ formation, as observed in previous studies [4], is not likely due to the exclusion of CO_2 in the gas environment.

A series of measurements at different humidity levels was performed at several temperatures (400–600 °C) in order to determine activation energies. The experimentally determined activation energy for oxygen surface exchange decreased by approximately 0.1 eV upon water exposure, as shown in Fig. 5. This reduction would predict $K_{wet} \approx 3.75*K_{dry}$, which is a larger improvement than we observe ($K_{wet} = 1.6–1.8*K_{dry}$). Considering the uncertainty in the activation energy calculation, this explains the increase in K′ reasonably well.

4. Conclusions

Under an applied cathodic electric field in the presence of humidified atmospheres, it is apparent that the steady-state out-of-plane strain, ξ_∞, of the LSCF film decreases, corresponding with an increase in the calculated effective ORR rate constant at the LSCF surface, relative to dry environments. Both trends, along with the commensurate observed decrease in overall cell resistance, suggest a counterintuitive improvement in cathode performance, which is in line with other short-term effects reported in the literature [19]. At short time scales, namely when oxygen vacancy transport is appreciable relative to cation transport, the Sr composition profile is constant and the presence of H_2O improves the oxygen transport kinetics at the cathode surface, manifesting as reduced resistance. The short-term beneficial humidification effect is dependent on both the degree of humidification and the cathodic polarization. Based on our DFT results for oxygen vacancy energies in the presence of water, we suggest that humidification results in surface hydroxyl groups that promote the transport of $V_{\ddot{O}}$ from the bulk lattice to the surface where the vacancies can participate in catalytic reactions. Assessing the effects of long-term humidity exposure,
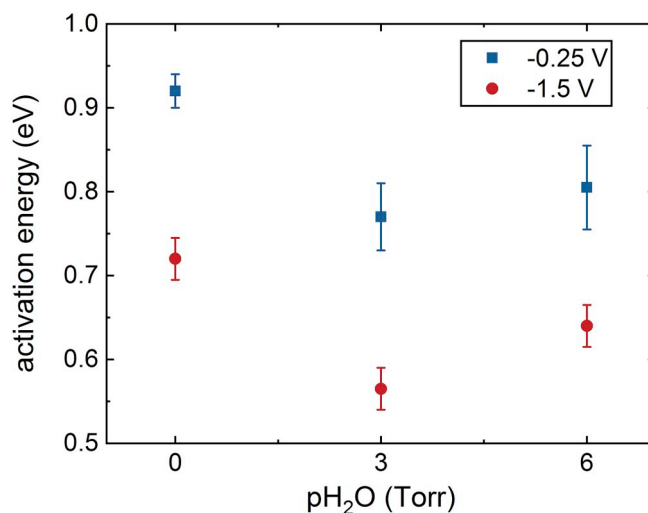

Fig. 5. Activation energy for surface exchange of oxygen vacancies in a dry O_2/Ar mixture and with 3 and 6 Torr H_2O. Error bars represent a 90% confidence interval.

which is known to have deleterious effects on the performance of SOFC cathodes and LSCF in particular, is outside the scope of the present investigation due to the time limitations of a synchrotron X-ray study.

Our results indicate that the water-induced short-term improvement in oxygen surface exchange stems from interactions of adsorbed hydroxyl groups with the cathode surface. If long term degradation of LSCF electrochemical properties can be prevented or mitigated, e.g., eliminating chromium transport from balance-of-plants components, water or other gas phase species could induce oxygen vacancy surface enrichment, which could be used to promote the oxygen reduction reaction at perovskite surfaces.

Author contributions

The manuscript was written through contributions from all authors. All authors have given approval to the final version of the manuscript.

Declaration of competing interest

The authors declare that they have no known competing financial interests or personal relationships that could have appeared to influence the work reported in this paper.

Appendix A. Supplementary data

Supplementary data to this article can be found online at https://doi.org/10.1016/j.jpowsour.2019.227478.

References

[1] S.B. Adler, Mechanism and kinetics of oxygen reduction on porous $La_{1-x}Sr_xCoO_{3-\delta}$ electrodes, Solid State Ion. 111 (1998) 125–134, https://doi.org/10.1016/S0167-2738(98)00179-9.

[2] T. Horita, K. Yamaji, N. Sakai, H. Yokokawa, T. Kawada, T. Kato, Oxygen reduction sites and diffusion paths in $La_{0.9}Sr_{0.1}MnO_{3-x}$/yttria-stabilized zirconia interface for different cathodic overvoltages by secondary-ion mass spectrometry, Solid State Ion. 127 (2000) 55–65, https://doi.org/10.1016/S0167-2738(99)00276-3.

[3] Y.L. Huang, C. Pellegrinelli, E.D. Wachsman, Fundamental impact of humidity on SOFC cathode ORR, J. Electrochem. Soc. 163 (2016) F171–F182, https://doi.org/10.1149/2.0221603jes.

[4] Z. Zhao, L. Liu, X. Zhang, W. Wu, B. Tu, D. Cui, D. Ou, M. Cheng, High- and low-temperature behaviors of $La_{0.6}Sr_{0.4}Co_{0.2}Fe_{0.8}O_{3-\delta}$ cathode operating under CO_2/H_2O-containing atmosphere, Int. J. Hydrogen Energy 38 (2013) 15361–15370, https://doi.org/10.1016/j.ijhydene.2013.09.089.

[5] T. Kawada, T. Horita, Cathodes, in: K. Kendall, M. Kendall (Eds.), High-Temp. Solid Oxide Fuel Cells 21st Century, Academic Press, New York, 2016, pp. 161–194.

[6] R.R. Liu, S.H. Kim, S. Taniguchi, T. Oshima, Y. Shiratori, K. Ito, K. Sasaki, Influence of water vapor on long-term performance and accelerated degradation of solid oxide fuel cell cathodes, J. Power Sources 196 (2011) 7090–7096, https://doi.org/10.1016/j.jpowsour.2010.08.014.

[7] E. Bucher, W. Sitte, F. Klauser, E. Bertel, Impact of humid atmospheres on oxygen exchange properties, surface-near elemental composition, and surface morphology of $La_{0.6}Sr_{0.4}CoO_{3-\delta}$, Solid State Ion. 208 (2012) 43–51, https://doi.org/10.1016/j.ssi.2011.12.005.

[8] E. Bucher, W. Sitte, F. Klauser, E. Bertel, Oxygen exchange kinetics of $La_{0.58}Sr_{0.4}Co_{0.2}Fe_{0.8}O_3$ at 600°C in dry and humid atmospheres, Solid State Ion. 191 (2011) 61–67, https://doi.org/10.1016/j.ssi.2011.03.019.

[9] J. Nielsen, A. Hagen, Y.L. Liu, Effect of cathode gas humidification on performance and durability of solid oxide fuel cells, Solid State Ion. 181 (2010) 517–524, https://doi.org/10.1016/j.ssi.2010.02.018.

[10] A. Hagen, K. Neufeld, Y.L. Liu, Effect of humidity in air on performance and long-term durability of SOFCs, J. Electrochem. Soc. 157 (2010) B1343–B1348, https://doi.org/10.1149/1.3459904.

[11] B.B. Ebbinghaus, Thermodynamics of gas phase chromium species: the chromium oxides, the chromium oxyhydroxides, and volatility calculations in waste incineration processes, Combust. Flame 93 (1993) 119–137.

[12] M. Krumpelt, T.A. Cruse, B.J. Ingram, J.L. Routbort, S. Wang, P.A. Salvador, G. Chen, The effect of chromium oxyhydroxide on solid oxide fuel cells, J. Electrochem. Soc. 157 (2010) B228–B233, https://doi.org/10.1149/1.3266930.

[13] S.J. Benson, D. Waller, J.A. Kilner, Degradation of La0.6Sr0.4Fe0.8Co0.2 O 3 − δ in carbon dioxide and water atmospheres, J. Electrochem. Soc. 146 (1999) 1305–1309, https://doi.org/10.1149/1.1391762.

[14] B. Hu, M. Keane, M.K. Mahapatra, P. Singh, Stability of strontium-doped lanthanum manganite cathode in humidified air, J. Power Sources 248 (2014) 196–204, https://doi.org/10.1016/j.jpowsour.2013.08.098.

[15] B. Hu, M.K. Mahapatra, V. Sharma, R. Ramprasad, N. Minh, S. Misture, P. Singh, Durability of lanthanum strontium cobalt ferrite $((La_{0.60}Sr_{0.40})_{0.95}(Co_{0.20}Fe_{0.80})O_{3-x})$ cathodes in CO_2 and H_2O containing air, Adv. Solid Oxide Fuel Cells Electron. Ceramics (2015) 75–82, https://doi.org/10.1002/9781119211501.ch8. John Wiley & Sons, Inc.

[16] V. Sharma, M.K. Mahapatra, S. Krishnan, Z. Thatcher, B.D. Huey, P. Singh, R. Ramprasad, Effects of moisture on (La, A)MnO_3 (A = Ca, Sr, and Ba) solid oxide fuel cell cathodes: a first-principles and experimental study, J. Mater. Chem. 4 (2016) 5605–5615, https://doi.org/10.1039/C6TA00603E.

[17] A. Nenning, E. Navickas, H. Hutter, J. Fleig, Water-induced decoupling of tracer and electrochemical oxygen exchange kinetics on mixed conducting electrodes, J. Phys. Chem. Lett. 7 (2016) 2826–2831, https://doi.org/10.1021/acs.jpclett.6b00778.

[18] Y.-L. Huang, A.M. Hussain, C. Pellegrinelli, C. Xiong, E.D. Wachsman, Chromium poisoning effects on surface exchange kinetics of $La_{0.6}Sr_{0.4}Co_{0.2}Fe_{0.8}O_{3-\delta}$, ACS Appl. Mater. Interfaces 9 (2017) 16660–16668, https://doi.org/10.1021/acsami.7b02762.

[19] J.H. Joo, R. Merkle, J. Maier, Effects of water on oxygen surface exchange and degradation of mixed conducting perovskites, J. Power Sources 196 (2011) 7495–7499, https://doi.org/10.1016/j.jpowsour.2011.04.032.

[20] B.J. Ingram, J.A. Eastman, K.-C. Chang, S.K. Kim, T.T. Fister, E. Perret, H. You, P. M. Baldo, P.H. Fuoss, In situ x-ray studies of oxygen surface exchange behavior in thin film $La_{0.6}Sr_{0.4}Co_{0.2}Fe_{0.8}O_{3-\delta}$, Appl. Phys. Lett. 101 (2012), 051603 https://doi.org/10.1063/1.4739518.

[21] E.M. Hopper, E. Perret, B.J. Ingram, H. You, K.-C. Chang, P.M. Baldo, P.H. Fuoss, J. A. Eastman, Oxygen exchange in $La_{0.6}Sr_{0.4}Co_{0.2}Fe_{0.8}O_{3-\delta}$ thin-film heterostructures under applied electric potential, J. Phys. Chem. C 119 (2015) 19915–19921, https://doi.org/10.1021/acs.jpcc.5b05505.

[22] P. Fuoss, K.-C. Chang, H. You, In situ X-ray studies of film cathodes for solid oxide fuel cells, J. Electron. Spectrosc. Relat. Phenom. 190 (2013) 75–83, https://doi.org/10.1016/j.elspec.2013.02.003. Part A.

[23] K.-C. Chang, B. Ingram, J. Ilavsky, S. Lee, P. Fuoss, H. You, Synchrotron X-ray studies of model SOFC cathodes, part I: thin film cathodes, Solid State Ion. 311 (2017) 118–126, https://doi.org/10.1016/j.ssi.2017.10.005.

[24] C.M. Folkman, M.J. Highland, E. Perret, S.K. Kim, T.T. Fister, H. Zhou, P.M. Baldo, S. Seifert, J.A. Eastman, P.H. Fuoss, D.D. Fong, Modular instrument mounting system for variable environment in operando X-ray experiments, Rev. Sci. Instrum. 84 (2013), 025111, https://doi.org/10.1063/1.4791799.

[25] G. Kresse, J. Furthmüller, Efficient iterative schemes for ab initio total-energy calculations using a plane-wave basis set, Phys. Rev. B 54 (1996) 11169–11186, https://doi.org/10.1103/PhysRevB.54.11169.

[26] G. Kresse, D. Joubert, From ultrasoft pseudopotentials to the projector augmented-wave method, Phys. Rev. B 59 (1999) 1758–1775, https://doi.org/10.1103/PhysRevB.59.1758.

[27] J.P. Perdew, K. Burke, M. Ernzerhof, Generalized gradient approximation made simple, Phys. Rev. Lett. 77 (1996) 3865–3868, https://doi.org/10.1103/PhysRevLett.77.3865.

[28] J. Hong, A. Stroppa, J. Íñiguez, S. Picozzi, D. Vanderbilt, Spin-phonon coupling effects in transition-metal perovskites: a DFT+U and hybrid-functional study, Phys. Rev. B. 85 (2012), 054417, https://doi.org/10.1103/PhysRevB.85.054417.

[29] W. Yang, Z. Wang, Z. Wang, C. Xia, R. Peng, X. Wu, Y. Lu, Enhanced catalytic activity toward O_2 reduction on Pt-modified $La_{1-x}Sr_xCo_{1-y}Fe_yO_{3-\delta}$; cathode: a combination study of first-principles calculation and experiment, ACS Appl. Mater. Interfaces 6 (2014) 21051–21059, https://doi.org/10.1021/am505900g.

[30] L. Wang, T. Maxisch, G. Ceder, Oxidation energies of transition metal oxides within the GGA+U framework, Phys. Rev. B 73 (2006) 195107, https://doi.org/10.1103/PhysRevB.73.195107.

[31] A.M. Ritzmann, J.M. Dieterich, E.A. Carter, Density functional theory + U analysis of the electronic structure and defect chemistry of LSCF ($La_{0.5}Sr_{0.5}Co_{0.25}Fe_{0.75}O_{3-\delta}$), Phys. Chem. Chem. Phys. 18 (2016) 12260–12269, https://doi.org/10.1039/C6CP01720G.

[32] W.C. Koehler, E.O. Wollan, Neutron-diffraction study of the magnetic properties of perovskite-like compounds $LaBO_3$, J. Phys. Chem. Solids 2 (1957) 100–106, https://doi.org/10.1016/0022-3697(57)90095-1.

[33] A.M. Ritzmann, M. Pavone, A.B. Munoz-Garcia, J.A. Keith, E.A. Carter, Ab initio DFT+U analysis of oxygen transport in $LaCoO_3$: the effect of Co^{3+} magnetic states, J. Mater. Chem. 2 (2014) 8060–8074, https://doi.org/10.1039/C4TA00801D.

[34] S.R. Bishop, K.L. Duncan, E.D. Wachsman, Defect equilibria and chemical expansion in non-stoichiometric undoped and gadolinium-doped cerium oxide, Electrochim. Acta 54 (2009) 1436–1443, https://doi.org/10.1016/j.electacta.2008.09.026.

[35] S.R. Bishop, K.L. Duncan, E.D. Wachsman, Thermo-chemical expansion in strontium-doped lanthanum cobalt iron oxide, J. Am. Ceram. Soc. 93 (2010) 4115–4121, https://doi.org/10.1111/j.1551-2916.2010.03991.x.

[36] S. Hashimoto, Y. Fukuda, M. Kuhn, K. Sato, K. Yashiro, J. Mizusaki, Thermal and chemical lattice expansibility of $La_{0.6}Sr_{0.4}Co_{1-y}Fe_yO_{3-\delta}$ (y = 0.2, 0.4, 0.6 and 0.8), Solid State Ion. 186 (2011) 37–43, https://doi.org/10.1016/j.ssi.2011.01.014.

[37] H. Ding, A.V. Virkar, M. Liu, F. Liu, Suppression of Sr surface segregation in $La_{1-x}Sr_xCo_{1-y}Fe_yO_{3-\delta}$: a first principles study, Phys. Chem. Chem. Phys. 15 (2013) 489–496, https://doi.org/10.1039/C2CP43148C.

[38] P.A.W. van der Heide, Systematic X-ray photoelectron spectroscopic study of $La_{1-x}Sr_x$-based perovskite-type oxides, Surf. Interface Anal. 33 (2002) 414–425, https://doi.org/10.1002/sia.1227.

[39] E.D. Wachsman, D. Oh, E. Armstrong, D.W. Jung, C. Kan, Mechanistic understanding of Cr poisoning on $La_{0.6}Sr_{0.4}Co_{0.2}Fe_{0.8}O_{3-\delta}$ (LSCF), ECS Trans. 25 (2009) 2871–2879, https://doi.org/10.1149/1.3205852.

[40] Y.A. Mastrikov, R. Merkle, E.A. Kotomin, M.M. Kuklja, J. Maier, Surface termination effects on the oxygen reduction reaction rate at fuel cell cathodes, J. Mater. Chem. A. 6 (2018) 11929–11940, https://doi.org/10.1039/C8TA02058B.

[41] Y. Cao, M.J. Gadre, A.T. Ngo, S.B. Adler, D.D. Morgan, Factors controlling surface oxygen exchange in oxides, Nat. Commun. 10 (2019) 1–15, https://doi.org/10.1038/s41467-019-08674-4.

[42] S.B. Adler, Factors governing oxygen reduction in solid oxide fuel cell cathodes, Chem. Rev. 104 (2004) 4791–4843.